Influence of the processing route on the mechanical properties of Cu–35Cr metal matrix composites

Lucas Varoto, Pierre Lhuissier, Jean-Jacques Blandin, Sophie Roure, Anthony Papillon, Mélissa Chosson, Guilhem Martin

Materials Science & Engineering A 908 (2024) 146953

Contents lists available at ScienceDirect

Materials Science & Engineering A

journal homepage: www.elsevier.com/locate/msea

Influence of the processing route on the mechanical properties of Cu–35Cr metal matrix composites

Lucas Varoto [a,b,*], Pierre Lhuissier [b], Jean-Jacques Blandin [b], Sophie Roure [a], Anthony Papillon [a], Mélissa Chosson [a], Guilhem Martin [b]

[a] Schneider Electric Industries, F-38000, Grenoble, France
[b] Univ. Grenoble Alpes, CNRS, Grenoble INP, SIMaP, F-38000, Grenoble, France

ARTICLE INFO

Keywords:
Cu-Cr metal matrix composites
Microstructures
Mechanical properties
Porosity
Interfaces

ABSTRACT

Cu–Cr-based composites with Cr content ranging from 20 to 50 wt% are widely used as electrical contacts for vacuum interrupters for medium voltage applications because of their excellent combination of mechanical, thermal, and electrical conductivity. Cu–Cr electrical contacts are usually processed by sintering or casting. Their mechanical properties have been the interest of some studies to enhance their percussion welding performance. However, a detailed microstructure-mechanical properties relationship for such composites is yet to be established. Herein, we report an in-depth multi-scale microstructural characterization of solid-state sintered and vacuum arc-remelted Cu–35Cr composites, coupled with the characterization of their mechanical properties. The strengthening mechanisms in both Cu and Cr phases are discussed in light of the microstructure differences caused by the processing route. The presence of large and interconnected pores at the Cu/Cr interfaces in the sintered Cu–Cr composites reduces the load transfer from the Cu matrix to the Cr reinforcing particles and leads to a lower dislocation density by differential thermal mismatch in the Cu matrix. We shed light on the influence of the processing routes on the microstructure-mechanical property relationships for Cu–35Cr composite materials.

1. Introduction

Cu–Cr-based alloys have been extensively explored for thermo-electrical applications because of their desirable combination of electrical, thermal, and mechanical properties. These properties result from a good electrical conductor, Cu, and a semi-refractory metal, Cr [1–3]. Their compositions vary significantly and accordingly with their application. Cu–Cr-based alloys with a Cr-content from 20 to 50 wt% have been widely used as electrical contacts in vacuum interrupters for medium voltage applications [4,5]. For such applications, besides the importance of high electrical and thermal conductivity to sustain thermo-electrical constraints, the mechanical properties of such alloys are also of extreme importance to sustain current breaking operations and percussion welding issues. Different manufacturing techniques have been used to produce these binary alloys, solid-state sintering (SSS), and vacuum-arc remelting (VAR) being the most widely used industrially. Because of the very limited solubility of Cr in Cu, these alloys can also be considered metal-matrix composites (MMC).

The microstructure of such composites varies significantly from one manufacturing technique to another. Cu–Cr-based composites issued from SSS show microstructures that are strongly dependent on the initial Cr powder employed (Cr-size and morphology) where the Cu-matrix can be considered as pure Cu [6–8]. In contrast, Cu–Cr-based composites inherited from solidification present a coarse dendritic Cr-primary with a Cu–Cr eutectic matrix [4,9,10]. Besides these microstructural differences, the Cu/Cr interfaces stand as one of the main differences between the composites resulting from those two different processing routes [11–13]. This is a key aspect when it comes to the properties of composite-based materials. It is well-known that the mechanical properties of MMC are the result of the different matrix-reinforcement interactions. Grain size (Hall-Petch), load bearing, high dislocation density induced by a difference in thermal expansion coefficients, Orowan strengthening, and porosity are factors affecting the mechanical properties of such MMC [14–17]. Consequently, the properties of the interfaces between the reinforcement and the matrix, here Cu/Cr interfaces, will play a key role in establishing such contributions in the

* Corresponding author. Schneider Electric Industries, F-38000, Grenoble, France.
E-mail address: lucas.varoto@grenoble-inp.fr (L. Varoto).

https://doi.org/10.1016/j.msea.2024.146953
Received 1 April 2024; Received in revised form 1 July 2024; Accepted 11 July 2024
Available online 14 July 2024

resulting mechanical properties [18–20].

The mechanical properties of Cu–Cr composites with high Cr content have been a subject of interest to enhance their performances, such as erosion resistance and resistance to percussion welding. For the latter, it has been pointed out that reducing the strength of Cu–Cr composites is beneficial to improving percussion welding issues [2,21,22]. Their mechanical properties, such as hardness and tensile properties are yet to be properly understood, especially concerning the effect of Cr content and size as well as the effect of additives on such properties [21–26]. In Cu–Cr alloys with a high Cr content, typically >10 %.wt, the main mechanical strengthening mechanism relies on the composite effect resulting from the reinforcement of the Cu matrix with harder Cr particles. Alloys with a lower Cr content, typically <5 wt% Cr, are strengthened via precipitation [1,3,27,28]. However, no detailed investigation of the microstructure-mechanical property relationships of such Cu–Cr with high Cr content composites is available yet, especially regarding the role of Cr-phase on such properties and their potential consequences on their performance, such as resistance to percussion welding. In addition, the comparison between SSS and vacuum-cast Cu–Cr materials has not been well documented. The discussion around the Cr-phase morphology and spatial distribution, the potential effects of the porosity, load-bearing effects as well as other key mechanical properties, such as yield strength, Young's modulus and elongation at fracture are not systematically reported for these Cu–Cr composites.

Herein, we shed light on the microstructure-mechanical property of Cu–35Cr MMC fabricated by two different processing routes: solid-state sintering (SSS) and vacuum-arc remelting (VAR) through a multiscale microstructural characterization. X-ray computed microtomography (XCT) was used to investigate in 3D the porosity, the Cr-phase size, morphology, and spatial distribution. Phase and orientation maps were collected at different scales using EBSD in the SEM and ACOM (Automated Crystallographic Orientation Mapping) in the TEM, respectively. The mechanical properties were probed at the macro and micro scale using hardness, tensile testing, and nanoindentation, and systematically compared with annealed pure copper. Based on these results, the strengthening mechanisms and their contribution to the mechanical properties are discussed.

2. Materials and methods

2.1. Materials

Cu–35Cr solid-state sintered (SSS) composites were directly supplied from Schneider Electric, Grenoble, France. These were fabricated by SSS under secondary vacuum. Pure dendritic copper powder and pure irregular chromium powder are mixed in a 65 %:35 % mass ratio. The Cu powder has an average equivalent diameter of 40 μm and the Cr powder has a particle size distribution from 30 to 80 μm in equivalent diameter. To maximize solid-state diffusion, the sintering heat treatment was performed at 1050 °C, near copper's melting point as reported in Ref. [6]. A final relative density of 96 % is achieved after sintering. Such a high density is considered the highest reachable density for such Cu–Cr composites using natural sintering. More details regarding the sintering parameters of Cu–Cr materials can be found in Ref. [6]. Cu–35Cr vacuum arc remelting (VAR) composites were directly supplied from Sirui Advanced Materials Co., Ltd, Xi'an, China. All the Cu–35Cr provided samples had a cylindrical shape with 80 mm in diameter and 8–10 mm in height. Both materials are in their as-fabricated state, no post-heat treatment was performed.

2.2. Microstructural characterization

2.2.1. X-ray computed tomography (XCT)

XCT was performed on cylindrical samples of 7 mm in height and 1 mm in diameter. Samples were prepared by electrical discharge machining out of Cu–35Cr SSS and VAR composites. An EasyTom XL laboratory tomograph from RX Solutions was used at 100 kV, with a 0.75 mm aluminum filter and 1.5 s acquisition per image with a total of 1792 projections. A volume of 1120 × 1120 × 1300 voxels was reconstructed by filtered back projection using the XAct software from RX Solutions. Under these conditions, each experimental setup resulted in a voxel size of 0.80 μm regardless of the samples analyzed. The spatial resolution enables the detectability of features, such as pores, as small as 3 μm in diameter and an accurate morphological description for features as small as 5 μm in diameter. Consequently, micron-sized Cr precipitates and small pores of about 1–2 μm in diameter were not captured in the XCT scans.

The reconstructed images were segmented using a machine-learning-assisted segmentation method presented and detailed in Ref. [29]. Then, the segmented images were analyzed using a specific image analysis procedure to investigate and quantify some microstructural characteristics of such composites. Different characteristics such as the size, morphology, geometrical percolation as well as the spatial distribution of both the Cr-phase and pores were analyzed. The characteristic size of each phase, Cu and Cr, was determined based on the 3D granulometry analysis using an octahedral structural element [30]. This results in an equivalent diameter size for the Cr-particles in the microstructure and a characteristic Cu-cord length, i.e., interparticle Cr–Cr characteristic distance. The geometrical percolation of the Cr-phase was evaluated by a 26-voxel connectivity labeling analysis. This means that all 26 neighbors of a Cr-voxel are considered in the labeling analysis. We have considered that the Cr-connections resulting from the segmentation are the result of effective Cr-inter particle contact, therefore, contributing to a geometrical percolation configuration. Thus, the result of the 26-connectivity labeling is used to estimate the percolation of the Cr-phase. For more details regarding the image analysis procedures, the interested reader is referred to Ref. [29].

2.2.2. Optical microscopy, scanning and transmission electron microscopy

Samples were prepared by mechanical polishing with 320 and 1200 SiC abrasive papers. Surface finishing was done using successively 9, 3, and 1 μm diamond suspensions. An additional vibratory polishing with a 0.03 μm colloidal silica solution for 4 h was employed as the final surface finishing step. Optical micrographs were taken with an Olympus BX51RF optical microscope equipped with the Olympus Stream Essentials imaging software. A Zeiss Gemini 500 FEG Scanning electron microscope (SEM) equipped with an Electron Backscattered Diffraction (EBSD) detector from EDAX was used. EBSD was performed using a step size of 0.2 μm to characterize the as-fabricated microstructure and a step size of 0.05 μm was used for the deformed microstructures. Note that in the EBSD maps, pixels having a confidence index (measures the local quality of the diffraction pattern) smaller than 0.1 were displayed in black in the maps. In addition, Kernel Average Misorientation (KAM) maps were calculated considering all points in the kernel and the 5 nearest neighbors. The average Grain Orientation Spread (GOS) of each phase in the as-fabricated and in the post-deformation states was calculated from the EBSD maps. For this, first, the misorientation between each neighboring pair of points (pixels) within each phase's grain is calculated. Then, the average misorientation value for each grain is determined and assigned to all the points (pixels) within the same grain. Therefore, all the grains in the Cu and Cr phases will have a value of the average misorientation resulting in a Grain Orientation Spread (GOS). The average for all the grains in Cu and Cr was thus calculated to obtain the average GOS of each phase. In addition, a lamella from each Cu–35Cr composite was extracted by Helios 5 PFIBCXe from ThermoFisher Scientific FIB. A tungsten mask was used to protect the material of interest from the etching and a Si-multipass at 15 nA was used to etch the surrounding material. Transmission Electron Microscopy (TEM) was performed on a JEOL 2100 Transmission Electron Microscope operation at 200 kV. The Energy-Dispersive X-ray Spectroscopy (EDS) was carried out on the same TEM using a high collection angle SDD Centurio detector. Images were acquired using Scanning Transmission Electron

Microscopy (STEM) mode. Automated Crystallographic Orientation Mapping (ACOM) in the TEM [31] was used with the hardware and software toolset ASTAR™ from Nanomegas to retrieve the local phase and orientation information. The step size was 2 nm. For more details regarding this technique, the reader is referred to Ref. [31].

2.2.3. Mechanical testing

Tensile specimens with a gauge length of 15 mm, a width of 3 mm and a thickness of 1.5 mm were machined out of the Cu–35Cr as-fabricated composites. Samples had an overall length of 45 mm with a grip section width of 10 mm. The tensile tests were conducted on an MTS 4 M machine (20 kN) equipped with a Digital Image Correlation (DIC) system from GOM Metrology. The tensile tests were performed under a constant strain rate of 0.001 s^{-1}. Three tensile tests were performed for each material to ensure the reproducibility of the mechanical response. The Young's modulus, Yield Strength taken at 0.2 % plastic strain, ultimate true tensile strength (UTS), uniform elongation determined using the Considère's criterion, and elongation at fracture were extracted from the stress-strain responses. The stress-strain response for the annealed pure Copper (ETP) is reproduced from Ref. [32]. Hardness Vickers was done using a load of 5 kgf and 15 s loading pause (HV/5/15) using an Innovatest IMP hardness tester. Nano-indentation mapping was performed using an Anton-Paar NHT3 tester at a constant strain rate of 0.05 s^{-1}, maximum load of 10 mN, and 10 s loading pause using a Berkovich type tip. A 20 × 20 indentation grid was made with a 10 μm spacing on the Cu–35Cr SSS and VAR composites to correlate the microstructure to Cr and Cu phases' mechanical properties. For this, the Oliver and Pharr model was used to estimate the hardness from indentation testing (nano-hardness) values [33].

3. Results

3.1. As-fabricated microstructures

3.1.1. Pores, phase morphology and spatial distribution of the Cr-phase

3.1.1.1. 2D observations. The typical microstructures of Cu–35Cr SSS and VAR alloys are shown in Fig. 1a–c and **b-d**, respectively. In the first case, the microstructure consists of coarse Cr-particles showing an irregular morphology embedded in a Cu-matrix. Because of the high Cr-content, i.e.35 wt%, which represents approximately 40 vol%, some Cr–Cr particle contacts can be observed. In addition, pores in the Cu matrix as well as Cu/Cr interfacial pores are still present after sintering. Some small and irregular Cr-precipitates, ranging between 1 and 5 μm in size, are also present due to Cr diffusion in Cu during sintering and precipitation during the subsequent slow cooling because of a reduced solubility of Cr in Cu at low temperatures (Fig. 1c). At high temperatures, over 900 °C up to the eutectic temperature of the Cu–Cr system (1076 °C), the maximum solubility of Cr in Cu can range from around 0.3 wt%Cr to 0.76 wt%Cr [34]. In the second case, the Cu–35Cr VAR microstructure is free of pores and consists of large Cr-rich particles (typically >20 μm) showing a dendritic morphology as well as a small Cr-eutectic phase (typically between 1 and 5 μm in size) embedded into a Cu-rich matrix. Spherical dark inclusions of 15 μm in size are found in the microstructure inherited from VAR, see Fig. 1b. The chemical nature of such inclusions will be further discussed in section 3.3.2. Besides the clear difference in Cr-phase morphology in SSS and VAR composite, its size and spatial distribution differ significantly. In the SSS composite, the Cr-phase is larger with greater Cr–Cr interspacing, around 50 μm and 100 μm respectively. In the VAR composite the Cr-phase is finer (about 10 μm) with significantly reduced Cr–Cr interspacing (nearly 20 μm). Such microstructural differences will be quantified based on XCT scans in the next subsection.

3.1.1.2. 3D observations. On the single 2D-cross sections of the reconstructed images from XCT shown in Fig. 2a–b, one can observe the same microstructural features as the ones observed in optical micrographs in Fig. 1a and **b**. Here, the following color code will be used to identify the main microstructural features of each composite after segmentation and 3D rendering: in the SSS composite interfacial pores are displayed in magenta, matrix pores in green, and Cr particles in dark grey while in the VAR composite, inclusions appear in red and the Cr-dendrites in dark grey. From Fig. 2a–b, both interfacial and matrix porosity can be easily distinguished as well as the Cr–Cr particle contacts for the Cu–35Cr sintered composite. In the Cu–35Cr composite fabricated by VAR, Cr-dendrites and inclusions can be clearly distinguished in the Cu-matrix. From the segmentation of the XCT images, these microstructural features can be represented in 3D as illustrated in Fig. 2c–h. In the Cu–35Cr sintered composite, large and interconnected Cu/Cr interfacial pores envelop Cr-particles while some spherical pores can be observed in the Cu-matrix. The quantification of such microstructural features results in a total volume fraction of porosity of 4.5 %, of which 95 % corresponds to interfacial porosity and only 5 % to matrix porosity. Throughout the volume fraction of Cr-particles analyzed, 95 % have an interfacial pore in its vicinity. In the Cu–35Cr VAR composite, no pore can be observed. Spherical inclusions are distributed randomly in the microstructure. The

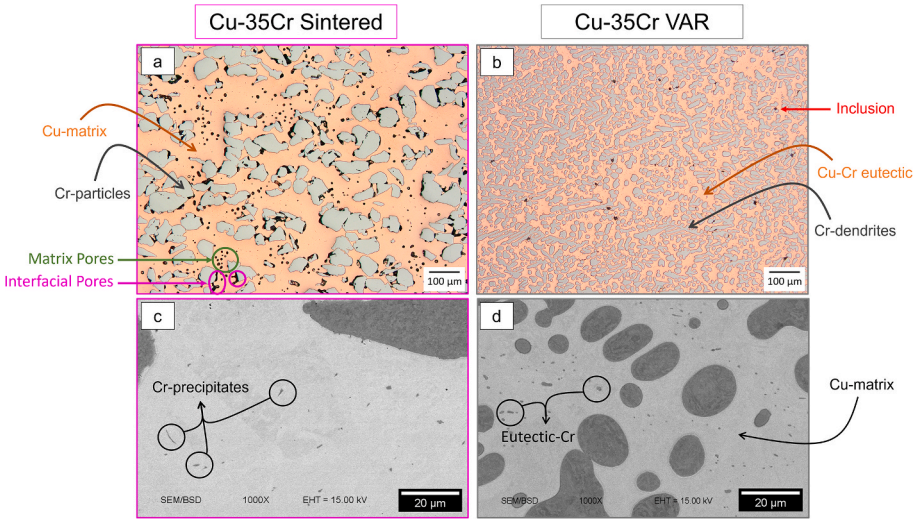

Fig. 1. Optical micrographs of the typical microstructure inherited from a) SSS, and b) VAR. SEM-BSE images showing enlarged views of the Cu-matrix; c) in the SSS sample, and b) in the sample inherited from VAR.

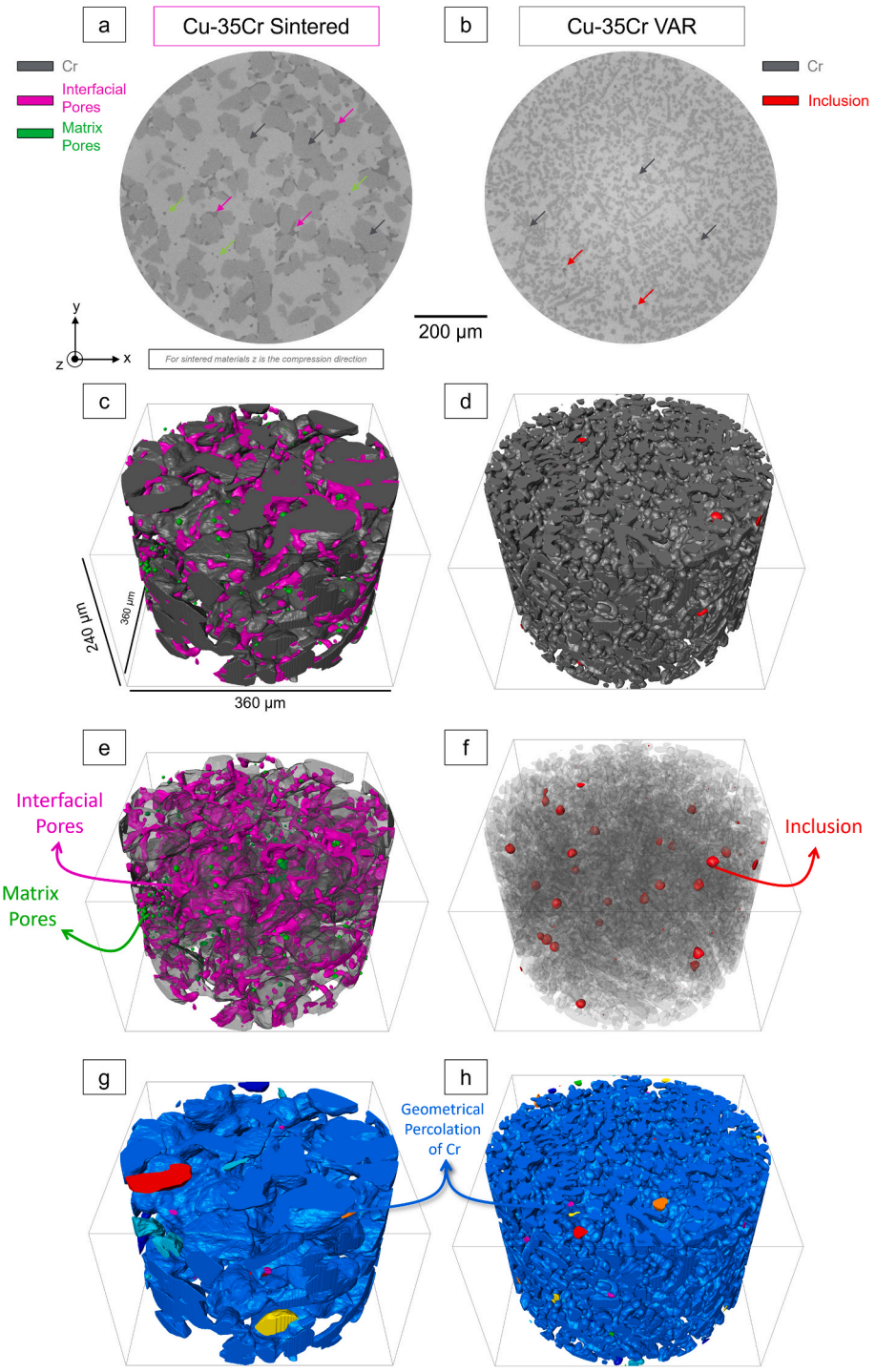

Fig. 2. 2D-cross sections of the reconstructed images from XCT for a) Cu–35Cr SSS composite and b) Cu–35Cr VAR composite showing the main microstructural features also observed on optical micrographs. c-d) 3D rendering of the microstructure (Cu-matrix in transparency) of a small volume of the total XCT reconstructed volume for the SSS and VAR composites, respectively. e-f) Same 3D rendering of c-d), respectively, with the Cr-phase in transparency showing the microstructural features, pores in e) and inclusions in f). g-h) Same small volume as in c-d) showing the Cr-phase percolation by labeling the Cr-phase with a 26-connectivity. Therefore, Cr particles with the same color can be considered in a Cr–Cr contact configuration and thus percolated. (For interpretation of the references to color in this figure legend, the reader is referred to the Web version of this article.)

volume fraction of the inclusions was determined to be around 0.15 vol % with an average size of around 15 µm in diameter and separated by an average first neighbor distance of 250 µm. Lastly, Fig. 2g–h shows the result of the 26-voxel connectivity analysis through the Cr-phase for both composites. Both Cu–35Cr SSS and VAR composites present fully light blue Cr-26-voxel connectivity in the volume analyzed, see Fig. 2g–h. Therefore, for both composites, the Cr-phase percolates geometrically creating a Cr-network in the Cu-matrix. The Cu phase is also found to be interconnected in the volume, the 35 wt%Cr (40 vol%) does not break the continuity of the Cu matrix.

The characteristic size of the Cr and Cu phases was estimated using a 3D granulometry analysis from the segmented microstructures. The cumulative distributions of the characteristic size in the Cr (equivalent diameter) and Cu (Cu-cord, i.e. interparticle Cr–Cr distance) phases are

given in Fig. 3. Considering the 0.5 percentile as an average value, one can see that there is a significant difference in the Cr-size phase in the VAR composite, around 10 μm, compared to SSS composite, with a Cr-size equivalent to around of 40 μm. Such a difference can also be seen in the Cu phase, where around 20 μm is found for the VAR composite while the average characteristic length of the Cu phase in the SSS composite is about 60 μm.

3.1.2. Phase and orientation mappings

3.1.2.1. At the microscale: ESBD maps. Fig. 4a–e shows the results of the EBSD characterization (IPF and phase maps) for both Cu–35Cr composites. The Cu grain size taken here as the average equivalent diameter varies from 25 ± 10 μm in the SSS composite to 15 ± 11 μm in the sample fabricated using VAR. One can see that the average size of Cu grains in the VAR composite is relatively close to the Cu characteristic size measured using the 3D analysis (around 15–20 μm) whereas in the SSS composite, the Cu characteristic size (60 μm) is more than 2 times higher than the Cu grain size. Both composites present a high density of annealing Σ3 twins in the Cu phase. Regarding the Cr-phase, EBSD maps show that Cr-particles in the SSS composite are polycrystalline. In addition, a significant misorientation within individual Cu grains and Cr phase can be noticed, especially in the Cu–35Cr VAR composite. Such results will be discussed later in sections 4.2.1 and 4.2.2.

The KAM maps in Fig. 5a–d highlight the local misorientation within the Cu-grains and Cr-phase in the materials processed by SSS and VAR from the EBSD data shown in Fig. 4a–f, respectively. Fig. 5e–f shows the cumulative misorientation profiles in the Cr-phase along the arrows in Fig. 5b and **d**. A clear difference in misorientation within both phases between the SSS and VAR composite is evidenced. This observation suggests the presence of a higher density of geometrically necessary dislocations (GNDs) within the as-fabricated microstructure of the VAR composite in comparison with the SSS composite. The misorientations observed in the VAR composite are particularly high near the interfaces. Regions with low misorientations are located in specific regions where long intercept lengths (typically >50 μm) in the Cu matrix are found. The regions circled with dashed black lines in Fig. 5c highlight examples of such regions. In the SSS composite, higher misorientation in the Cu and Cr phases can be observed in the regions where Cr-clusters are present, see the boxes highlighted using dashed lines in Fig. 5a. The difference in misorientation in the Cr-phase is evident from the misorientation profiles from the arrows displayed in Fig. 5b and **d**. While the Cr-phase in the SSS composite presents nearly misorientation-free Cr-particles, except locally where a Cr-clustering can be found, higher misorientations can be seen in the VAR composite, see the misorientation profiles Fig. 5e and **f**. This can also be reflected by the average of the misorientation angles to the mean grain orientation, also called grain orientation spread (GOS), calculated in each phase in both composites. The average GOS in the Cu and Cr phases are respectively estimated at 1.0 and 0.6° in the SSS sample, and 4.3 and 4.3° in the composite processed by VAR. The average GOS of the Cu and Cr-phase in the VAR composite is approximately four and seven times greater than in the SSS composite in the as-fabricated state, respectively.

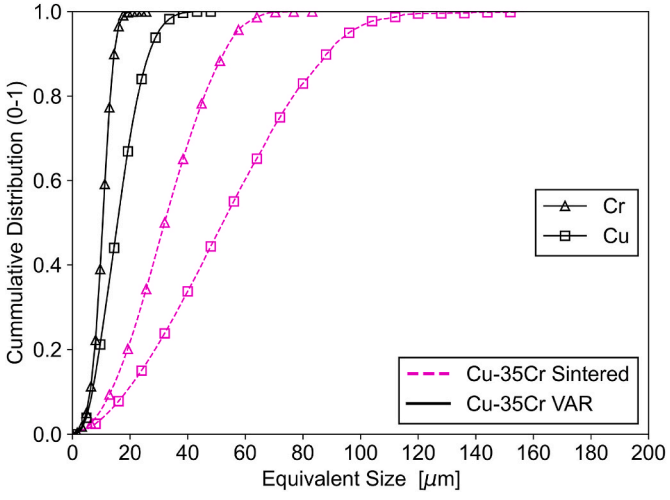

Fig. 3. Cumulative Distribution Functions for the equivalent size of each phase, Cu and Cr, for VAR and SSS Cu–35Cr composites.

3.1.2.2. At the nanoscale: ACOM maps. Downscaling the microstructural characterization of both Cu–35Cr composites, Fig. 6a–f shows the transmission electron microscopy results where the two phases present in such composites can be observed. Fig. 6b and f correspond to a virtual bright field (VDF). VDF images are generated by selecting one or numerous diffraction spots to highlight, i.e. enhance the contrast of the selected phase and the non-selected phase [31]. For such STEM images, the diffraction spots from Cu and Cr were selected. Both the phase and orientation maps resulting from ACOM analyses for each microstructure are shown in Fig. 6c–d and **g-h**. For the Cu–35Cr SSS alloy, a single Cr particle and a fraction of Cu-matrix can be easily distinguished. The Cr-phase is free of dislocations and fine precipitates. For the Cu–35Cr VAR alloy, two adjacent secondary Cr-dendritic arms are observed with a fraction of Cu-matrix in between. Surprisingly, a high density of dislocations as well as a significant number of fine precipitates (<100 nm) can be found in the Cr-dendrites in the Cu–35Cr VAR sample. The misorientation inside the dendrite arms can also be noticed, see the orientation map in Fig. 6h. Some dislocations can also be observed in the Cu-matrix in between the Cr-dendrites arms. Fig. S1 in the supplementary materials provides additional STEM bright field images of Fig. 6a and **e** with a different tilt, confirming the presence of a much higher density of dislocations in the VAR composite. Note that no orientation relationship between the Cu matrix and the Cr reinforcing particles was found regardless of the composite (VAR or SSS).

Fig. 7a–f is a detailed STEM analysis of the fine precipitates observed in the Cr-dendrites in the VAR composite including crystallographic information from ACOM and chemical information from EDS. The experimental diffraction spots along with the matching patterns from ACOM analysis are displayed in Fig. 7d–f. The associated EDS maps are given in Fig. 7b–c. The EDS maps confirm that such fine precipitates are Cu-rich precipitates, see Fig. 7d–f. The indexed diffraction spots from the selected regions in Fig. 7a match relatively well with the Cr-BCC and the Cu-FCC phase respectively embedded into the Cr-dendrite, see Fig. 7d–f. One can conclude that these fine precipitates are Cu-rich precipitates embedded in the Cr-phase. Their size is smaller than 100 nm. No orientation relationship between the Cu-rich precipitates and the Cr-phase was observed.

3.2. Mechanical properties of Cu–35Cr composites

3.2.1. Microscale mechanical properties: nano-hardness mapping

Fig. 8a–b shows the 20 × 20 nano-indentation grid onto the microstructure, i.e. contours of the Cr-phase, with the hardness map overlayed for both Cu–35Cr composites. The corresponding optical micrographs of the microstructures containing the grid of indentations are shown in Figs. S2a and b. In addition, Fig. 8c shows the average hardness in each phase (Cu and Cr) as well as the standard deviation in both composites. Note that to estimate the average hardness in each phase, the values of indentations near the Cu/Cr interface or near the inclusion in the VAR sample were not considered (Fig. 8b). As expected, there is a clear difference in hardness for the Cr-phase compared to the Cu matrix. Consequently, the hardness map fits relatively well with the optical micrographs, i.e. the hardness map correlates well with both Cu–35Cr microstructures. Interestingly, the average Cu-phase hardness is similar in both composites. However, one can notice a difference in hardness in

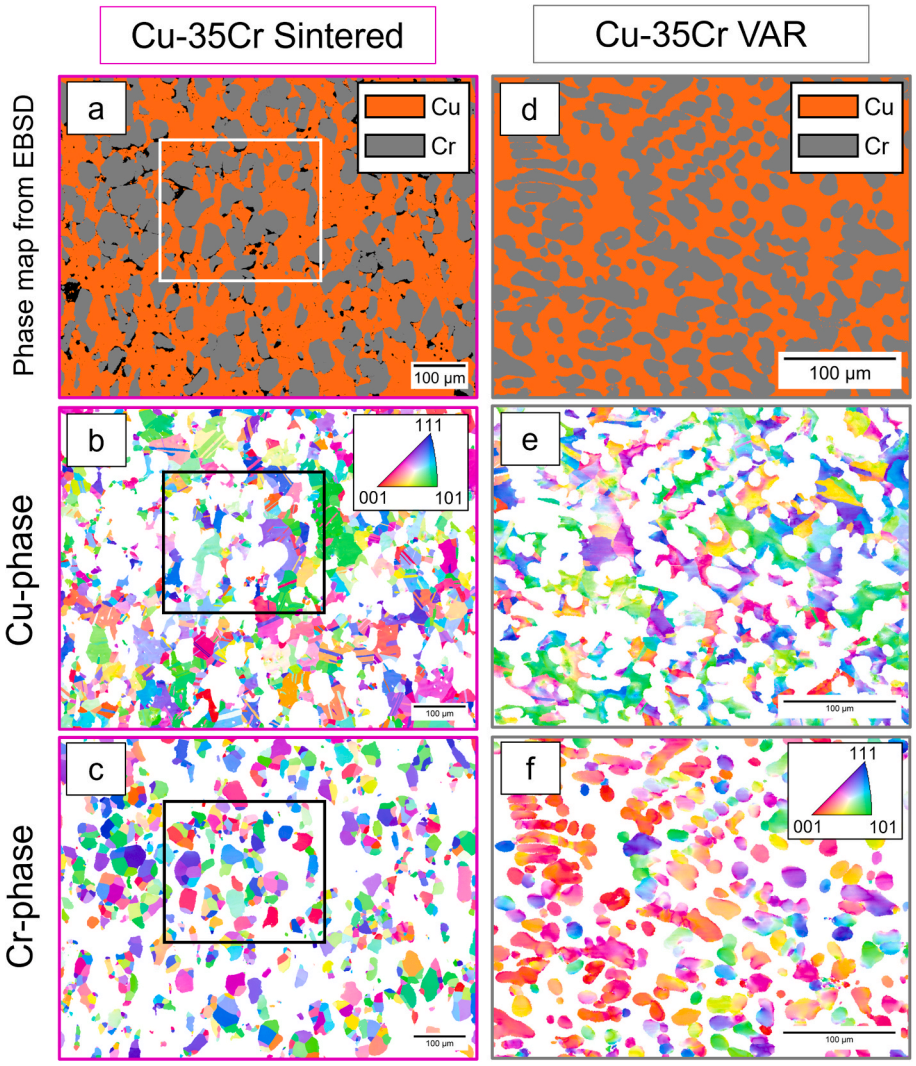

Fig. 4. a-d) Phase map from EBSD. b-c) and e)-f) EBSD-inverse pole figure maps of the Cu-phase and Cr-phase for the Cu–35Cr SSS and VAR composite, respectively.

the Cr-phase when comparing the VAR and SSS samples, the Cr-phase in the VAR sample being nearly 20 % harder than the Cr-phase in the SSS sample. The average hardness in the Cr-phase of the VAR composite reaches 4300 MPa while for the SSS composite, it is around 3500 MPa. High values of nano-hardness in the VAR composite, typically >6000 MPa, are associated with the presence of inclusions as illustrated in Fig. 8b.

3.2.2. Macroscale mechanical properties: Hardness and tensile response

The hardness (HV/5) of pure annealed Cu-ETP, Cu–35Cr SSS, and VAR composite is given in Table 1. There is a significant increase in hardness, by a factor of 2, from pure annealed copper to Cu–35Cr VAR composite. This is not the case for the Cu–35Cr SSS, where there is only a limited increase in hardness compared to pure annealed Cu.

The tensile response and the tensile properties for both Cu–35Cr composites as well as for annealed pure Cu-ETP are shown in Fig. 9a–c, respectively. The Young's modulus, Yield Strength, Ultimate Tensile Strength (UTS), the elongation to failure as well as the uniform elongation are given. The average value is given at the top of each bar chart in Fig. 9c. From these results, on can see that Cu–35Cr VAR composite presents a higher Young's Modulus, Yield Strength and UTS compared to the Cu–35Cr SSS composite and pure annealed Cu-ETP. As for the SSS composite, only its Yield Strength is higher than pure annealed copper's. The latter presents an elongation at fracture and a uniform elongation superior to both composites. Note that such experimental results for the mechanical properties from the tensile tests agree with those found in the literature and for the SSS composite, no superior mechanical properties have been reported [2,21].

3.3. Deformed microstructures

3.3.1. EBSD characterization

EBSD IPF and KAM maps of the post-deformation microstructures for the SSS and VAR composites are shown in Fig. 10a–j. Such maps were acquired at approximately 3 mm from the fracture surface, in the region subjected to uniform deformation, i.e. far away from the region affected by necking. Since there is no significant difference in uniform deformation between VAR and SSS composites, one can consider that such EBSD maps are collected in microstructures deformed to relatively similar plastic strains. The misorientation profiles in the Cr-phase for both composites are shown in Fig. 10e and **j**. Both Cu and Cr-phases present a high misorientation distribution due to plastic deformation. After deformation, the Cr-phase in the VAR composite shows a higher misorientation compared to the Cr-phase in the SSS composite, see KAM maps in Fig. 10d and **i**. This is evidenced by the misorientation profiles displayed in Fig. 10e and **j**. In the Cr-phase in the VAR composite, a significantly higher misorientation degree from 15° up to 40° is present whereas such values hardly reach a maximum of 15° in the Cr-phase in the SSS composite. Such differences in misorientation, suggesting a difference in plastic deformation in both phases from one composite to

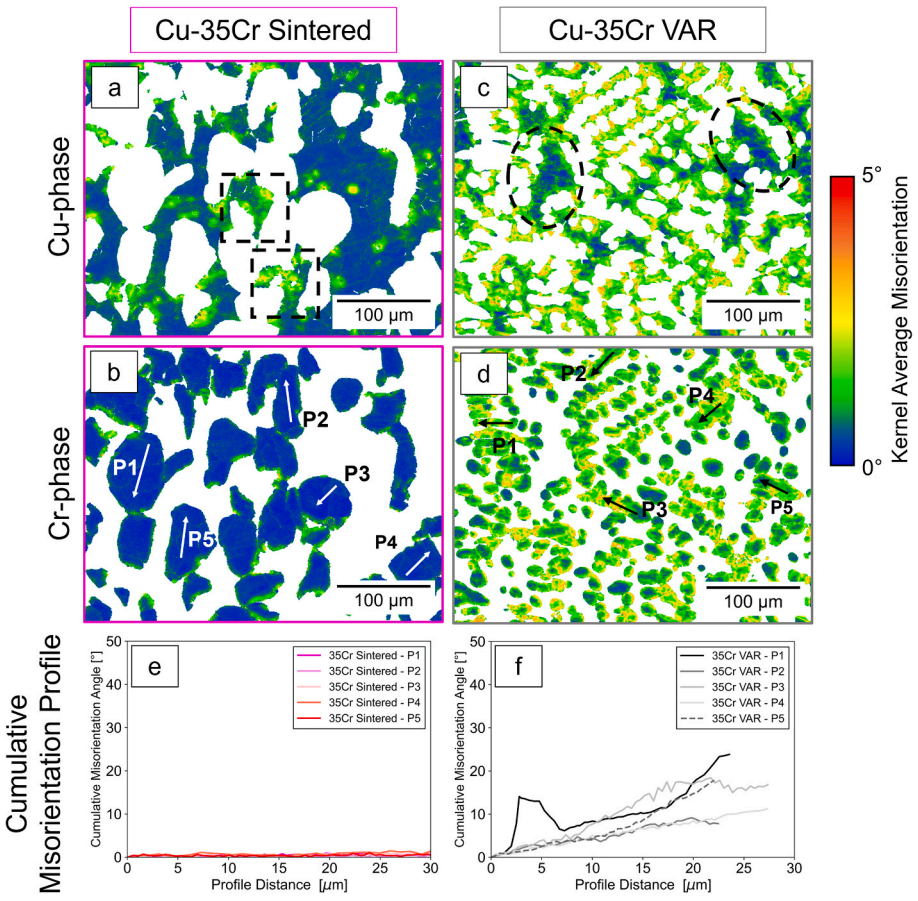

Fig. 5. a-d) Kernel Average Misorientation (KAM) map of the Cu-phase and Cr-phase for the Cu–35Cr SSS and VAR composite. e-f) Cumulative misorientation profiles in the Cr phase measured along the arrows drawn in b) and d).

the other, are also reflected by the average grain orientation spread (GOS) in each phase of both composites after deformation. The average GOS in the Cu and Cr-phase after deformation are measured at 3.8° and 2.8°, respectively, in the sample fabricated by SSS. In the VAR sample, the average GOS in the Cu matrix and Cr phase are respectively estimated at 6.3° and 5.8°.

3.3.2. *Damage and fractography*

Fig. 11a–c shows the fracture surface from the tensile specimens for both Cu–35Cr composites. On the one hand, in the Cu–35Cr SSS composite three coexisting modes of fractures can be observed. First, relatively large, and conical shape dimples are present in the Cu matrix. Second, brittle fracture of the Cr phase by cleavage is observed. Finally, de-bonding of the Cr-particles can also be detected in the fracture surface, see Fig. 11a. The latter results from the growth and coalescence of the preexisting interfacial pores. On the other hand, the fracture surface of the Cu–35Cr VAR composite exhibits dimples in the Cu matrix with the presence of inclusions in some dimples and traces of Cr-cleavage, see Fig. 11b–c. Fig. 12a–d shows the sample side surfaces near the fracture surface for both materials. The large voids present near the Cu–Cr interfaces in the Cu–35Cr SSS composite can be considered the signature of the growth of the preexisting interfacial pores contributing to the fracture, see Fig. 12a and **c**. In the VAR composite, the fracture of the Cr-phase, and the inclusion-initiated fracture are also evidenced, see Fig. 12b–d. An EDS-spectrum of the inclusion in the VAR composite microstructure reveals an Al and O-rich inclusion. We suggest that such inclusions are alumina inclusions resulting from the fabrication process.

4. Discussion

4.1. *Difference in Young's modulus between Cu–Cr VAR and SSS composites*

The elastic modulus of particulate metal matrix composites is the result of complex and non-linear interactions between the constituent phases [35]. Different models based on the principles of linear elasticity, such as the Hashin and Shtrikman bounds (HS lower and upper bounds, HS-LB and HS-UB respectively), self-consistent estimates, mean field theories as well as finite element modeling have been proposed to estimate the elastic properties of metal matrix composites.

In the case of Cu–35Cr composites, the contribution of the elastic properties of Cu (E_{Cu} = 120 GPa [1], μ_{Cu}=45 GPa) and Cr ($E_{Cr} \approx$ 280 GPa [36], μ_{Cr}=110 GPa) would result in HS bounds for the elastic modulus of a Cu–35Cr composite ranging from 170 GPa (HS-LB) and 180 GPa (HS-UB). From the rule of mixture approach, such bounds are 160 (LB) to 187 GPa (UB), respectively. From the stress-strain response, the elastic modulus of Cu–35Cr VAR and SSS composites were measured at 152 ± 22 GPa and 75 ± 11 GPa, respectively. From the HS or rule of mixture analytical models, one can suggest that the value measured experimentally for the Cu–35Cr VAR composite is in relative agreement considering the experimentally estimated error associated (±22 GPa), whereas that for the Cu–35Cr SSS composite is significantly lower than the predictions. The effect of pores at the interfaces between the matrix and the particles on the elastic properties in particulate metal matrix composite was investigated by Mochida et al. [37]. From an analytical model that combines Eshelby's equivalent inclusion method and Mori-Tanaka's back stress analysis, they proposed an adapted analytical model to account for such an effect on the elastic properties. Such a

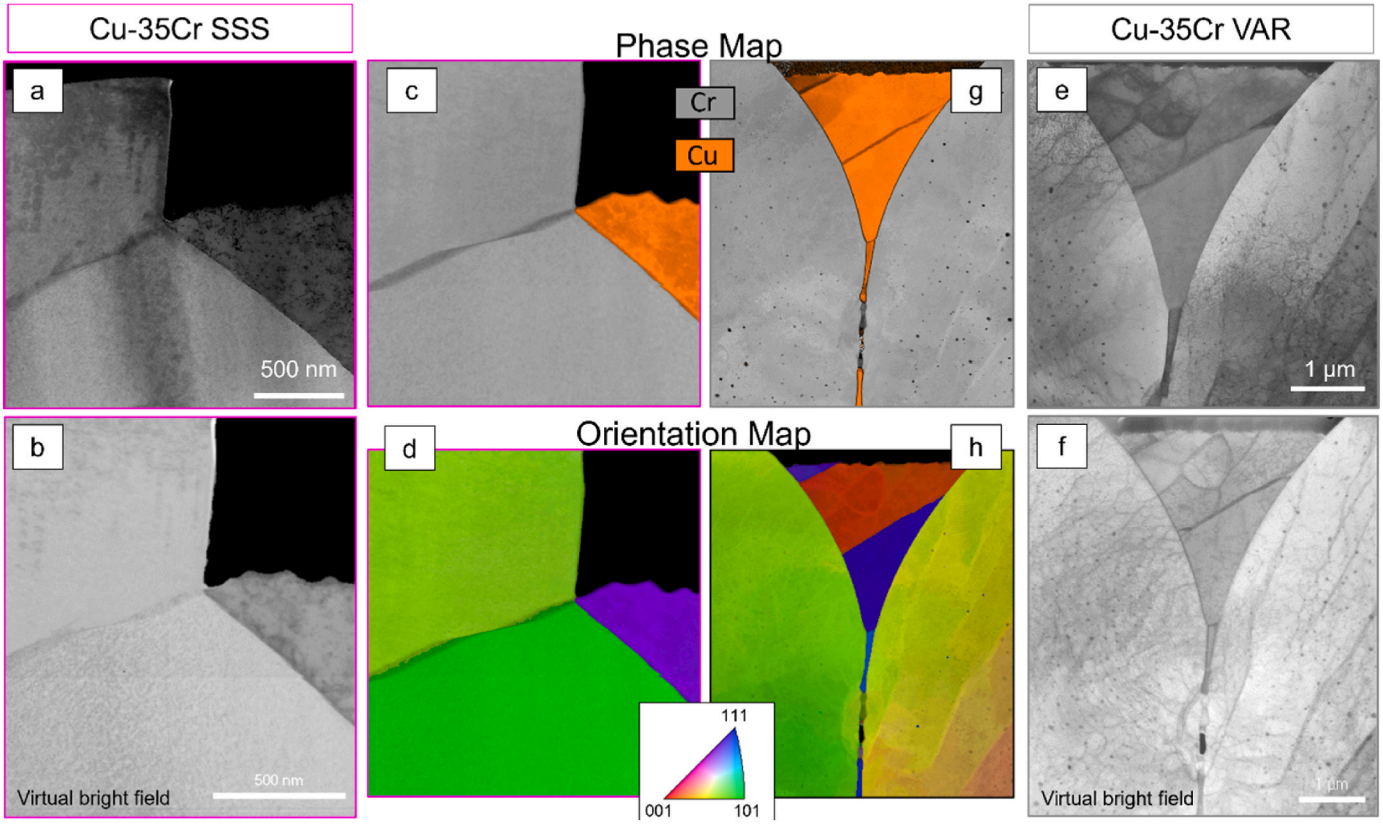

Fig. 6. a and e) STEM observations of the microstructure of Cu–35Cr SSS and VAR composite, respectively, where both phases, Cu and Cr are present followed by their corresponding b and f) virtual bright field STEM image. c) and g) and d and h) The phase map and orientation map from ACOM-ASTAR™ for Cu–35Cr SSS and VAR, respectively.

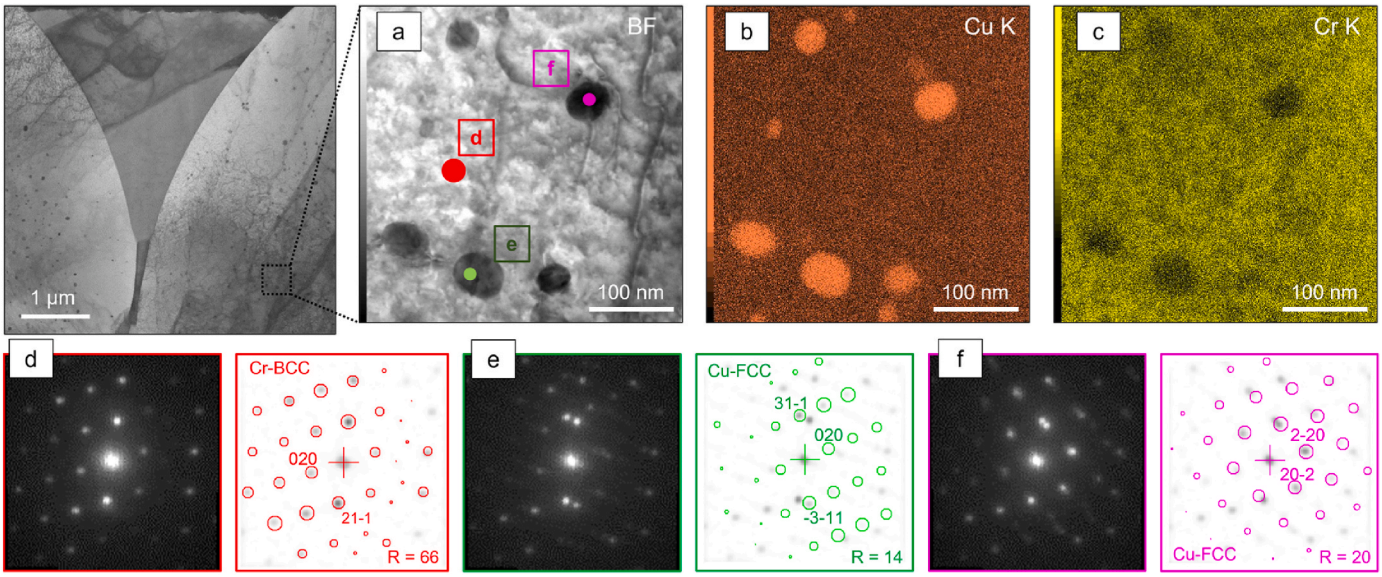

Fig. 7. a) Bright field STEM image of a selected region of interest located in the Cr-dendrite from VAR composite showing the nanosized Cu-rich precipitates; b-c) Corresponding EDS-STEM elemental mapping for Cu and Cr; d-f) the experimental diffraction patterns at the points indicated in a) followed by their crystallographic indexing using ACOM-ASTAR™.

model expresses the ratio between the elastic modulus of the composite, E_c, and the elastic modulus of the matrix, E_m, by the expression [37]:

$$\frac{E_c}{E_m} = \frac{1}{1 + \eta_P^{III}(1 - V_d)V_P + \eta_3 V_P V_d} \quad (1)$$

where η_P^{III} and η_3 are functions that depend on the Eshelby's tensor and on the elastic stiffness tensor of the matrix and the reinforcement particles as well as the initial volume fraction of particles, V_P, and the volume fraction of debonded particles, V_d. For more details of such formulation, see Ref. [37].

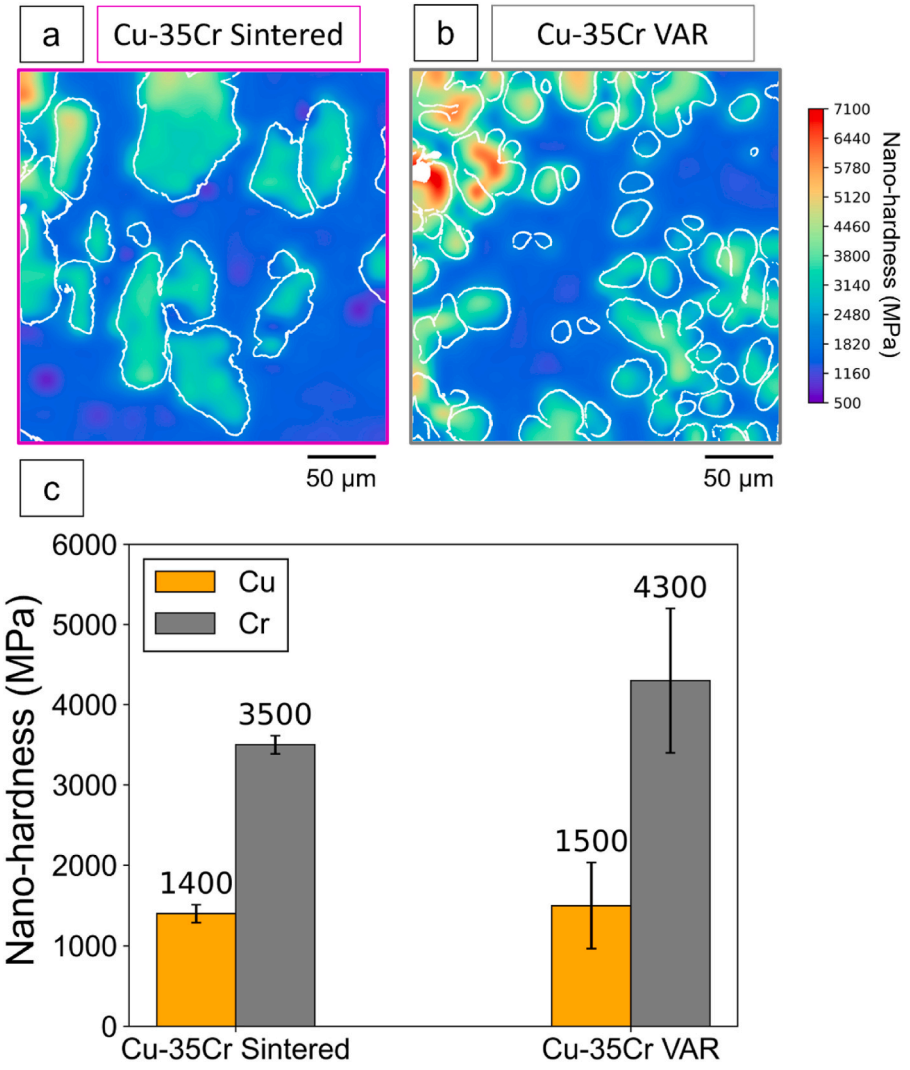

Fig. 8. a-b) Optical micrographs of the microstructure of Cu–35Cr SSS and VAR composite where the indentations are overlaid with the nano-hardness; c) Bar chart showing the average hardness in each phase (Cu and Cr) in both composites.

Table 1
Average Vickers hardness (HV/5) values for pure annealed Copper-ETP, and Cu–35Cr SSS and VAR composites.

Alloy	HV/5
Cu-ETP annealed	46 ± 1 ref. [32]
Cu–35Cr SSS	60 ± 4
Cu–35Cr VAR	97 ± 3

From the experimental results, one can consider the elastic modulus ratio $\frac{E_{sss}}{E_{VAR}} = 0.5$ as the reference ratio between a Cu–35Cr composite containing Cr-debonded particles and a Cu–35Cr composite without the presence of Cr-debonded particles, i.e., Cu–35Cr VAR. According to Mochida's model, a total of 75 % volume fraction of debonded Cr-particles would yield a $\frac{E_c}{E_m} = 0.5$. From the XCT images and segmentation, the quantified volume fraction of Cr particles containing an interfacial pore in its vicinity is approximately 95 %. In this case, the corresponding reduced elastic modulus ratio from the Mochida's model would decrease by an additional 10 % in comparison with the experimental results. Considering the error associated with the experimental calculation of the elastic modulus for Cu–35Cr SSS composite (±11 GPa), one can consider the difference between the elastic modulus ratio from Mochida's model and the one found by the XCT not significant. Thus, the presence of interfacial porosity is thought to be the main mechanism responsible for the reduced elastic modulus of the Cu–35Cr SSS composite.

4.2. Difference in strengthening mechanisms

4.2.1. Strengthening mechanisms in the Cu-matrix

Hereafter, we discuss the strengthening mechanisms involved in the Cu matrix of the Cu–35Cr SSS and VAR metal matrix composites which may result from different mechanisms. The various strengthening contributions in the Cu matrix are estimated and discussed in an effort to weigh each of them with respect to the Cu–35Cr SSS and VAR composites' yield strength and nano-hardness within the Cu phase. The objective is to weigh the different sources of strengthening in the Cu matrix. We rely on the multi-scale microstructure characterization previously presented to define some inputs to estimate the relative contributions to the strength of the Cu matrix. Table 2 gives a summary of all the constants used hereafter to estimate contributions to the yield strength of the Cu matrix.

The increase of the yield strength of the Cu matrix, σ_y^{Cu}, results from different microstructural strengthening contributions, such as the grain boundaries (Hall-Petch), solid solution strengthening, forest hardening caused by the high dislocation density resulting from the difference in

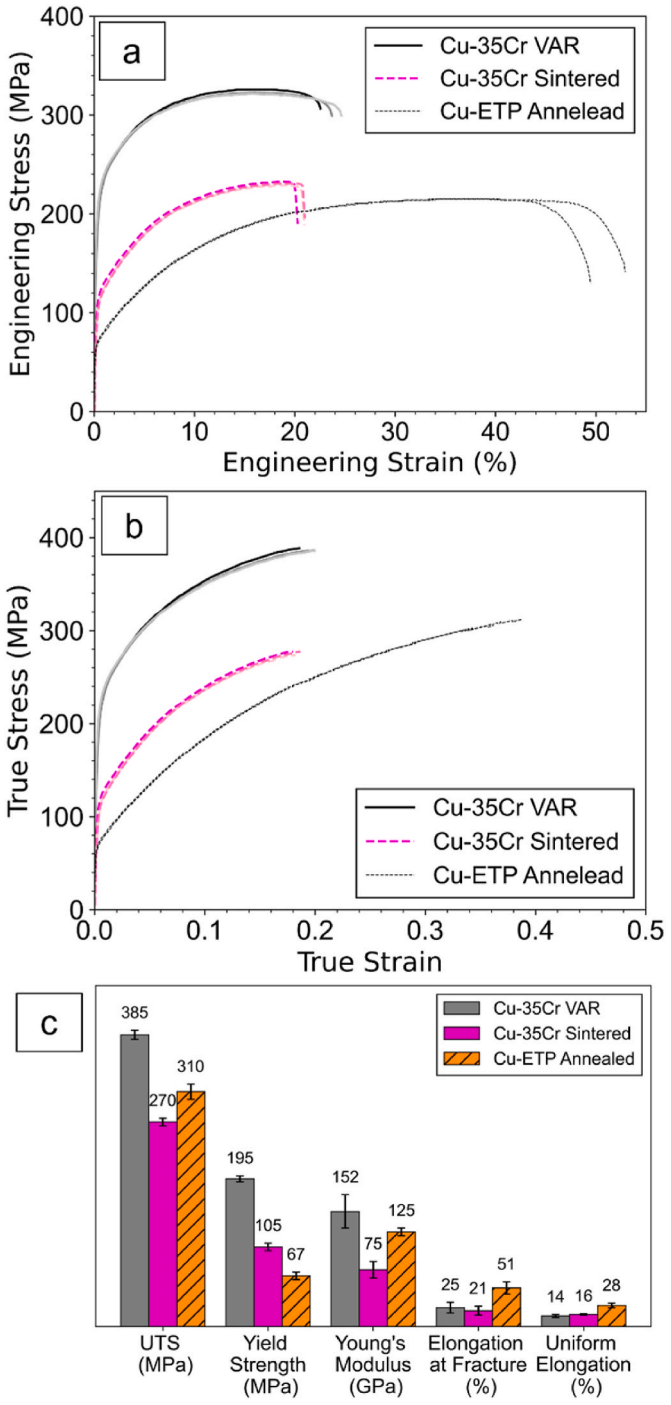

Fig. 9. a) Typical example of Engineering Stress-Strain and b) True Stress-True Strain tensile curves for Cu–35Cr SSS, VAR, and pure annealed Cu-ETP; c) Young's Modulus, Yield Strength, Ultimate Tensile Strength (UTS), and Elongation to failure (measured on the engineering stress-strain tensile response) and Uniform Elongation (determined using the Considère criterion) extracted from b).

coefficients of thermal expansion between Cu and Cr, and precipitation strengthening. In the simplest case, where no synergistic effect is considered between such contributions, σ_y^{Cu} can be estimated by an addition law, see equation (2):

$$\sigma_y^{Cu} = \sigma_{o-Cu} + \Delta\sigma_{y-GB} + \Delta\sigma_{y-Solid-Solution} + \Delta\sigma_{y-Dislocation\ by\ CTE} + \Delta\sigma_{y-Precipitation} \quad (2)$$

As demonstrated previously the Cu–35Cr VAR composite microstructure does not present defects such as Cu/Cr interfacial porosity or Cu-matrix pores (Fig. 2). Thus, one may consider such a case as the reference Cu–35Cr composite microstructure to evaluate the strengthening contributions in the Cu matrix. First, the average grain size of the Cu-phase in the Cu–35Cr VAR composite was determined to be about 15 μm from the EBSD analysis shown in Fig. 4. Thus, the grain boundary strengthening contribution in the matrix can be estimated based on the Hall-Petch relationship: $\Delta\sigma_{y\text{-}GB} = k_1 d^{0.5}$. This gives a contribution of 35 MPa.

The solid solution strengthening can be estimated from the relation derived in Refs. [39–41] and given in equation (3):

$$\Delta\sigma_{y-Solid-Solution} = M\left(\frac{3}{8}\right)^{\frac{2}{3}}\left(\frac{1+\nu}{1-\nu}\right)\left(\frac{w}{b}\right)^{\frac{1}{3}} G \times \sum_i \left|\varepsilon_i\right|^{4/3} c_i^{2/3} \quad (3)$$

where c_i is the concentration of element i in solid solution. The maximum solubility of Cr in solid solution in Cu near the eutectic temperature (around 0.76 wt% [42,43,34]) results in a maximum solid solution strengthening of approximately 30 MPa (upper bound). However, considering that the cooling inherent of VAR and SSS fabrication process and the negligible solubility of Cr in Cu at room temperature does not favor the solid solution of Cr in Cu, one can assume that the solid solution is depleted and consequently, the strengthening contribution can be considered negligible.

The increase in dislocation density induced by thermal mismatch, i.e. different coefficients of thermal expansion (CTE), between the matrix and the second phase has been widely investigated in several metal matrix composites [14–16,44–47]. Here, thermal plastic strains accommodate the different expansion-contraction behaviors from the matrix and the particulate reinforcement during cooling from the high-temperature heat treatment or from the high fabrication temperature. The strengthening effect on the Cu matrix resulting from the dislocation density caused by the thermal mismatch in metal matrix composites where the reinforcing particles are assumed to deform elastically can be estimated using equation (4) taken from Ref. [15]:

$$\Delta\sigma_{y-Dislocation\ by\ CTE} = \alpha\mu b\rho^{\frac{1}{2}}, with\ \rho = \frac{V_P^{\frac{4}{3}}\Delta CTE\Delta T}{bl(1-V_P)} \quad (4)$$

where l stands for the equivalent mean particle radius. From the XCT results, the average equivalent diameter in the Cr-phase was approximately 10 μm. Thus, we took an average radius of the particle l equal to 5 μm in the above expression. With the premise that the microstructure suffers from thermal mismatch from the eutectic temperature (1070 °C) to ambient temperature and the difference of coefficient of thermal expansion between Cu and Cr is constant through cooling, $\Delta CTE \approx 10 \times 10^{-6}\ K^{-1}$[48,49], one can estimate a contribution from the dislocations resulting from the thermal mismatch of about 80 MPa.

The precipitation strengthening may have different mechanisms contributing to enhancing the yield strength of the Cu matrix. Order strengthening by ordered coherent precipitates, coherency strengthening, Modulus hardening due to the different elastic modulus between the matrix and the precipitate, and Orowan strengthening by obstacles not sheared by dislocations are usually the main mechanisms to such contribution [50]. As previously discussed, for Cu–35Cr VAR composites, given the size of the Cr-eutectic phase (between 1 and 5 μm) in the Cu matrix [43,51], one can neglect the precipitation strengthening mechanism contribution in the Cu matrix of the Cu–35Cr VAR composite.

In the case of the Cu–35Cr SSS composite, the average grain size of the Cu-phase from the EBSD analysis allows the estimation of a Hall-Petch contribution of 25 MPa (very close to its equivalent in the VAR composite). The solid solution and precipitation strengthening contribution can also be neglected in this case. The effect of porosity on the yield strength could eventually be taken into account by the empirical

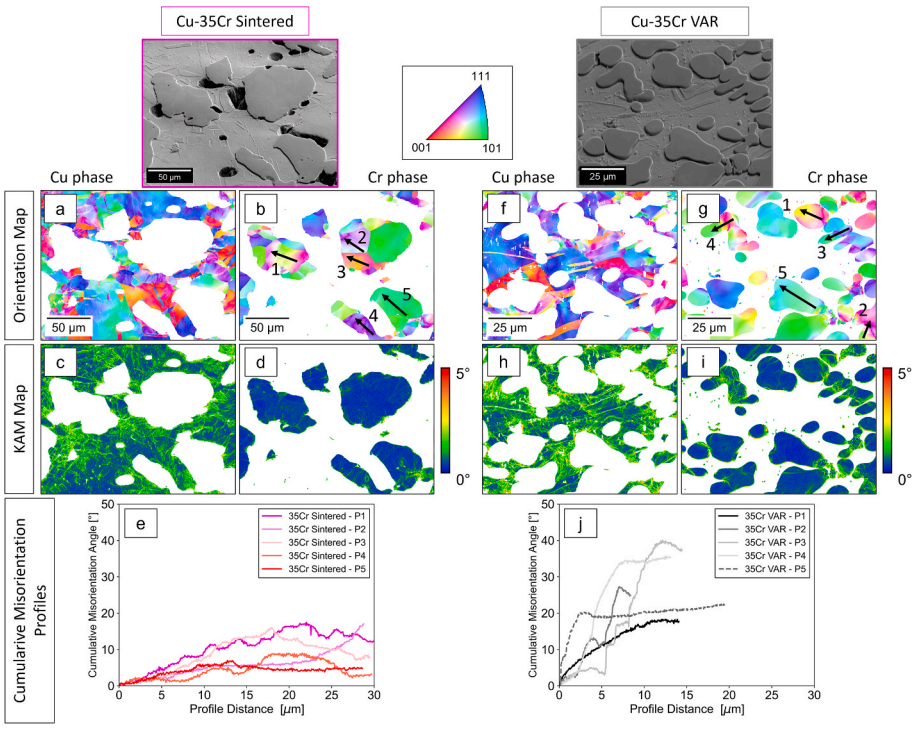

Fig. 10. a-b) and f-g) IPF Orientation maps and c-d) and h-i) the corresponding KAM maps collected in deformed samples, e-f) Misorientation profiles along the arrows indicated in the orientation maps b) and g) in the post-deformation microstructures, for both composites.

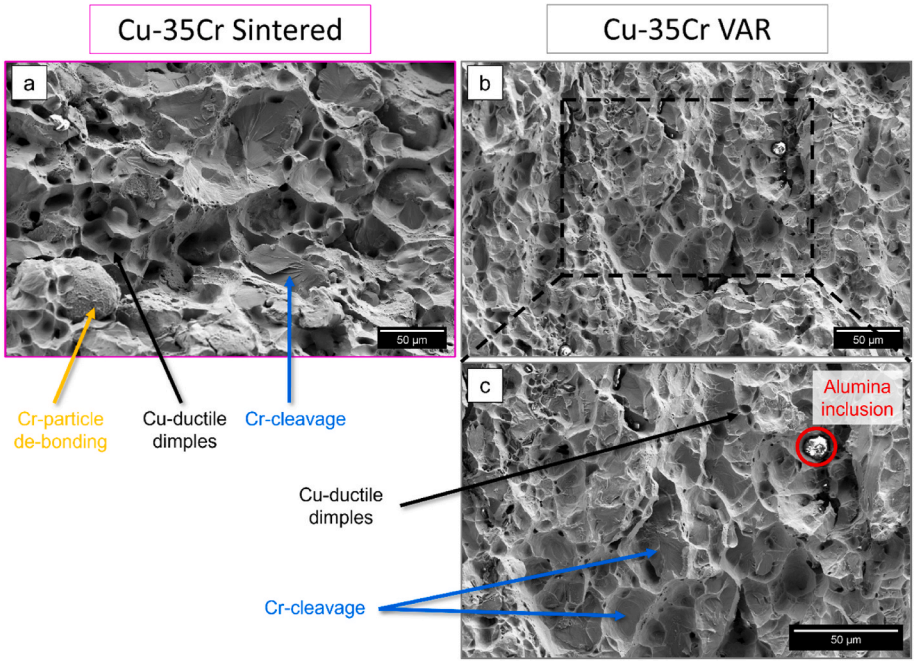

Fig. 11. SEM images of the fracture surfaces from Cu–35Cr composites: a) solid-state sintered and b-c) VAR composite.

expression proposed in Refs. [52,53]. However, as 5 % (0.2 vol% absolute) of the total volume fraction of porosity corresponds to Cu-matrix porosity one can neglect the negative contribution of porosity in the Cu matrix. The KAM maps and the STEM images collected in the as-fabricated microstructures show that the Cu–35Cr SSS microstructure contains a reduced density of GNDs, compared to Cu–35Cr VAR composites, see the KAM maps in Fig. 5a–d. Here, the effect of the difference in CTE between Cu and Cr during cooling from the high sintering temperature is hindered by the presence of large and interconnected Cu/Cr interfacial pores evidenced in the XCTs images. Such interfacial pores envelop Cr particles, leaving only a fraction of the surface area in contact with the Cu-matrix. This isolates the Cr-particles from the Cu-matrix. This strongly limits the creation of GNDs at the interface by the thermal mismatch. One can, thus, suggest that only a fraction of the potential strengthening effect by high dislocation density is achieved. As a result, the reduction in yield strength of the Cu–35Cr SSS composite compared to the VAR composite is thought to be partly caused by the significant reduction of dislocation strengthening in the Cu-matrix.

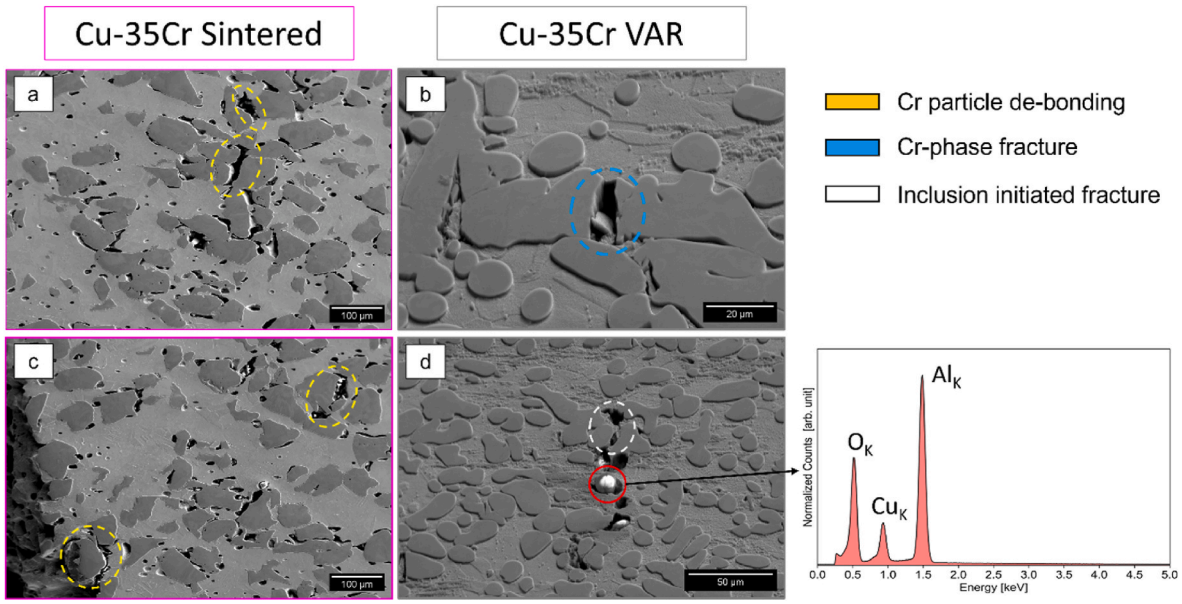

Fig. 12. Microstructure near the fracture surface of the Cu–35Cr tensile test specimens; a-c) SSS composite; b-d) VAR composite. EDS spectra on the right show the constituent elements of the inclusion present in the Cu–35Cr VAR microstructure, assumed to be Alumina inclusions.

Table 2
Summary of all the constants used in this work to estimate the various strengthening contributions to the yield strength.

Parameters			Refs.
σ_{o-Cu} (MPa)	Friction stress of Cu	20	[17]
k_1 (MPa.m$^{1/2}$)	Hall Petch parameter	0.14	[17]
M	Taylor factor for a random texture	3.06	
ν	Poisson ratio of Cu	0.34	[1]
G_{Cu} (GPa)	Shear modulus of Cu	45	[17]
G_{Cr} (GPa)	Shear modulus of Cr	110	[36]
ΔG	Shear modulus mismatch between Cu and Cr	65	
b (nm)	Burgers vector of Cu	0.256	[17]
$w = 5b$ (nm)	Interaction force parameter	1.28	
ε_{Cr} (%)	Misfit strain for Cr	1.3	[38]
α	Constant for dislocation strengthening	0.3	[14–16]

Considering the various sources of strengthening in the Cu matrix, the Cu matrix of the SSS composite seems to be much softer than the one of the VAR composite. At first sight, this is not consistent with our nano-hardness measurements that rather show a slightly harder Cu matrix in the VAR composite in comparison with the SSS composite, see Figs. 8c and 9c. Indeed, one would expect a more pronounced difference in nano-hardness (as in yield strength), due to the clear difference in dislocation density between the Cu matrix in the VAR and SSS composites. However, we noticed a large standard deviation in the VAR sample in comparison with the SSS composite. We suggest that this large standard deviation in the VAR composite results from the size of the indentation grid that covers only a limited area that may not be a representative, and the fact that we ignored the indentations in close vicinity of the Cu/Cr interfaces when estimating the average indentation hardness in the Cu matrix. By doing so, we therefore do not necessarily capture the short-range heterogeneity in dislocation density illustrated in Fig. 5c.

In addition to the previously discussed strengthening mechanisms in the Cu-matrix, load bearing between the composite's constituent phases plays an important role in the mechanical behavior [47,54]. Given the significant interfacial porosity volume fraction in the SSS composite, load transfer from the Cu-matrix to the reinforcing Cr-particles is strongly hindered, limiting its strengthening contribution. In the VAR composite, due to the absence of Cu/Cr interfacial pores interface, load transfer is more efficient and accounts for an estimated 195 (YS) – 135 (from the previous Cu—matrix strengthening mechanisms) = 60 MPa.

4.2.2. *Strengthening mechanisms in the Cr-phase*

The Cr-phase in the VAR Cu–35Cr composite shows an average hardness 20–30 % higher than that of the SSS composite with also a larger standard deviation. The Cr-phase in the VAR composite presents a significantly higher misorientation compared to its counterpart in the SSS composite (Figs. 5 and 6). In addition, the STEM observation shown in Fig. 6 highlights a surprising and significant number of dislocations in the Cr-phase of the VAR composite, see also Fig. S1 in supplementary materials. This is an interesting observation that is worth reflecting on. Indeed, in the literature dedicated to MMCs [14–16,44–47], the presence of a high density of dislocations in the matrix is attributed to the difference in coefficient of thermal expansion (CTE) between the matrix and the reinforcing particles that are assumed to deform elastically. However, the possible plastic deformation of the reinforcing phase has drawn much less attention. Although dislocations observed in the Cr phase in the VAR composite will not per se compensate for differential thermal shrinkage, their formation may be attributed to thermal stresses if these have a deviatoric component also within the convext Cr phase, for example due to elastic anisotropy in Cu and Cr crystals making the composite. In the case of the VAR microstructure, there is no interfacial pores and several Cu grains with different orientations surround the Cr-dendrites (Fig. 4e), thus elastic anisotropy might be held responsible for the heterogeneous deformation fields revealed in Fig. 5. However, this assumption would require further investigations to clarify how elastic anisotropy in the Cu phase can affect the local deformation heterogeneities and induce plasticity in the Cr dendrites.

In the Cr-phase in the Cu–35Cr SSS composite, because of the presence of a large and significant fraction of Cu/Cr interfacial porosity, there is no need to compensate for differential thermal shrinkage by plastic deformation of the Cr phase, leaving a near dislocation density-free Cu-matrix and Cr-phase. It is worth mentioning the observation of globular Cu precipitates within the Cr phase with a size >50 nm [55]. Considering their size and incoherency, we suggest that the strengthening contribution of such Cu precipitates to dislocation motion is limited. From this, we concluded that the higher average of indentation hardness value in the Cr phase of the VAR composite results mainly from the presence of a high density of dislocations while the Cr phase in the SSS composite contains a very low density of dislocations as illustrated

by the misorientations in the Cr in both composites, see Figs. 5–7.

4.3. Damage mechanisms

In the Cu–35Cr VAR composite, the fracture surfaces shown in Fig. 12b–c indicate that the damage mechanisms are similar compared to the SSS composite, however, no pre-existing interfacial Cu/Cr voids were observed, revealing the better Cu/Cr interface properties. Smaller dimples can be found in the Cu-matrix, which deform around the Cr-phase. In addition, Cr-phase damage is characterized by the brittle fracture with Cr-cleavage or the presence of inclusion within some dimples. Due to the stronger Cu/Cr interface, the load transfer from the Cu matrix to the Cr reinforcement is more efficient, evidenced by the misorientation profiles in Fig. 11f–j. It is worth mentioning that the presence of large spherical inclusions may play a detrimental role in the damage evolution of the Cu–35Cr VAR composite contributing to a localized source of voids and cracks formation during deformation (Fig. 12c).

From the fracture surfaces shown in Fig. 12a, large and conical-shaped dimples can be observed in the Cu-matrix, cleavage fracture in the Cr-phase, and the growth and coalescence of the pre-existing interfacial pores for the Cu–35Cr SSS composite. In this case, the presence of pores in the Cu-matrix acts as stress concentration sites. Such pores serve as microplasticity initiation sites and contribute to the coalescence of voids from the ductile behavior of the Cu-matrix, forming large and conical shape dimples. In addition, with the evolution of deformation, the Cu/Cr interfacial pores grow and eventually coalesce resulting in Cr-particles debonding. This latter shares the damage mechanism with localized and limited Cr-particle breaking, as Fig. 12a shows by the cleavage surfaces on the Cr-particles. This leads to the reduced ductility and uniform elongation of the Cu–35Cr SSS composite compared to the VAR composite though the latter one shows a higher strength.

5. Conclusions

The microstructure-mechanical property relationships of Cu–35Cr composites fabricated by two different routes, namely SSS and VAR were investigated. An in-depth microstructural characterization using an array of characterization techniques (XCT, SEM/EBSD, TEM) followed by mechanical testing including nanoindentation mapping, microhardness and tensile testing allowed the relationships between the microstructure and the mechanical properties of such Cu–Cr metal matrix composites to be clarified. Such results shed light on the optimization of the mechanical properties of such Cu–Cr composites used as electrical contacts to enhance their mechanical performance, such as percussion welding. The main conclusions of this work can be summarized:

- The inherent SSS and VAR Cu–35Cr microstructures show different microstructural features. Cu/Cr interfacial and matrix porosity in the particulate Cu–35Cr SSS and the dendritic and percolative Cr-phase in the Cu–35Cr VAR composite stands as the main microstructural differences.
- Cu–35Cr VAR composite presents higher mechanical properties, with a higher elastic modulus (152 GPa in the VAR composite vs. 75 GPa in the SSS composite), yield strength (195 MPa in the VAR vs. 105 MPa in the SSS), and ultimate tensile strength (385 MPa in the VAR vs. 270 MPa in the SSS) compared to the Cu–35Cr SSS composite.
- High dislocation density by thermal mismatch is the main source of strengthening in the Cu-matrix for Cu–35Cr VAR composite. Load bearing also contributes significantly to the strengthening of the Cu-matrix. Cu/Cr interfacial porosity attenuates such mechanisms for the SSS composites, producing a near dislocation-free Cu-matrix from thermal mismatch and hindering load bearing effect. Such interfacial pores are responsible for reducing SSS composites' elastic modulus, yield strength, ultimate tensile strength, and ductility.
- The presence of a high dislocation density and fine Cu-rich precipitates in the Cr-phase of the Cu–35Cr VAR composite contributes to additional strengthening mechanisms compared to dislocation and precipitates-free Cr-phase in the SSS composite. The presence of a high dislocation density in the Cr phase of the VAR composite might result from plastic deformation driven by deviatoric stress fields induced by differential thermal shrinkage of elastically anisotropic Cu and Cr crystals during cooldown of the composite after processing.

CRediT authorship contribution statement

Lucas Varoto: Writing – original draft, Visualization, Validation, Methodology, Investigation, Formal analysis, Data curation, Conceptualization. **Pierre Lhuissier:** Writing – review & editing, Validation, Supervision, Methodology, Investigation, Data curation, Conceptualization. **Jean-Jacques Blandin:** Writing – review & editing, Visualization, Validation, Supervision, Methodology. **Sophie Roure:** Writing – review & editing, Validation, Supervision, Project administration. **Anthony Papillon:** Writing – review & editing, Validation, Supervision, Project administration. **Mélissa Chosson:** Writing – review & editing, Visualization, Validation. **Guilhem Martin:** Writing – review & editing, Visualization, Validation, Supervision, Project administration, Methodology, Investigation, Conceptualization.

Declaration of competing interest

The authors declare that they have no known competing financial interests or personal relationships that could have appeared to influence the work reported in this paper.

Data availability

Data will be made available on request.

Acknowledgments

The authors are grateful to Schneider Electric Industries and Association Nationale de la Recherche Technologique (ANRT) for the financial support of this work in the framework of the PhD of Lucas Varoto (CIFRE 2021/1619). The authors are also grateful to Stephane Coindeau, from the Grenoble INP - CMTC characterization platform, Marc Fivel and Charles Josserond for the technical and experimental support of the XCT experiments, nano-indentation, and tensile test experiments, respectively.

Appendix A. Supplementary data

Supplementary data to this article can be found online at https://doi.org/10.1016/j.msea.2024.146953.

References

[1] J.R. Davis, Copper and Copper Alloys, ASM Specialty Handbook, ASM International, 2001. ISBN: 0-87170-726-8.
[2] P.G. Slade, The Vacuum Interrupter: Theory, Design, and Application, CR Press Taylor & Francis Group, Boca Raton, 2008. ISBN 978-0-8493-9091-3.
[3] H. Tang, Z. Ma, C. Lei, et al., High strength and high conductivity Cu alloys: a review, Sci. China Technol. Sci. 63 (2020) 2505–2517, https://doi.org/10.1007/s11431-020-1633-8.
[4] J. Han, Z. Dou, T. Zhang, W. An, Review of the recent Chinese research on the electrical properties of CuCr contacts for vacuum interrupters, J. Mater. Res. Technol. 25 (2023) 1585–1598, https://doi.org/10.1016/j.jmrt.2023.06.060.
[5] W. Huang, H. Yu, L. Wang, X. Wu, C. Ouyang, Y. Zhang, J. He, State of the art and prospects in sliver- and copper-matrix composite electrical contact materials, Mater. Today Commun. 37 (2023) 107256, https://doi.org/10.1016/j.mtcomm.2023.107256.
[6] A. Papillon, et al., Sintering mechanisms of Cu-Cr metallic composites, Int. J. Refract. Met. Hard Mater. 65 (2017) 9–13, https://doi.org/10.1016/j.ijrmhm.2016.11.010.

[7] K.v. Klinski-Wetzel, C. Kowanda, M. Heilmaier, F.E.H. Mueller, The influence of microstructural features on the electrical conductivity of solid phase sintered CuCr composites, J. Alloys Compd. 631 (2015) 237–247, https://doi.org/10.1016/j.jallcom.2014.12.249.

[8] S. Spaić, M. Komac, A. Fetahagić, Microstructure and properties of sintered Cu–25Cr alloy, Mater. Sci. Technol. 5 (1989) 1069–1073, https://doi.org/10.1179/mst.1989.5.11.1069.

[9] R. Muller, Arc-melted Cu-Cr alloy as contact materials for vacuum interrupters, Siemens Forsch.- Entwicklungsberichte 17–33 (1988) 105–111.

[10] C.Y. Zhang, Y.P. Wang, Z.M. Yang Z M, Y. Guo, B.J. Ding, Microstructure and properties of vacuum induction melted CuCr25 alloys, J. Alloys Compd. 366 (2004) 289–292, https://doi.org/10.1016/j.jallcom.2003.07.001.

[11] B. Miao, H. Guo, Y. Zhang, G. Liu, W. Wang, Effects of interface characteristics of Cu/Cr phases on the contact performance of Cu-25Cr alloy contact material, in: 23rd International Symposium on Discharges and Electrical Insulation in Vacuum, 2008, pp. 185–188, https://doi.org/10.1109/DEIV.2008.4676750.

[12] T. Gong, P. Yao, X. Xiong, H. Zhou, Z. Zhang, Y. Xiao, L. Zhao, M. Deng, Microstructure and tribological behavior of interfaces in Cu-SiO2 and Cu-Cr metal matrix composites, J. Alloys Compd. 786 (2019) 975–985, https://doi.org/10.1016/j.jallcom.2019.01.255.

[13] B. Miao, Y. Zhang, G. Liu, Current status and developing trends of Cu-Cr contact materials for VCB, in: XXIst International Symposium on Discharges and Electrical Insulation in Vacuum, 2004. Proceedings. ISDEIV., 2004, pp. 311–314, https://doi.org/10.1109/DEIV.2004.1422608.

[14] V.C. Nardone, K.M. Prewo, On the strength of discontinuous silicon carbide reinforced aluminum composites, Scripta Metall. 20 (1986) 43–48, https://doi.org/10.1016/0036-9748(86)90210-3.

[15] B. Derby, J.R. Walker, The role of enhanced matrix dislocation density in strengthening metal matrix composites, Scripta Metall. 22 (1988) 529–532, https://doi.org/10.1016/0036-9748(88)90019-1.

[16] R.J. Arsenault, N. Shi, Dislocation generation due to differences between the coefficients of thermal expansion, Mater. Sci. Eng. 81 (1986) 175–187, https://doi.org/10.1016/0025-5416(86)90261-2.

[17] Niels Hansen, Hall–Petch relation and boundary strengthening, Scripta Mater. 51 (2004) 801–806, https://doi.org/10.1016/j.scriptamat.2004.06.002.

[18] E.A. Feest, Interfacial phenomena in metal-matrix composites, Composites 25 (1994) 75–86, https://doi.org/10.1016/0010-4361(94)90001-9.

[19] K.E. Aifantis, J.R. Willis, The role of interfaces in enhancing the yield strength of composites and polycrystals, J. Mech. Phys. Solid. 53 (2005) 1047–1070, https://doi.org/10.1016/j.jmps.2004.12.003.

[20] Guoqing Wu, Qingqing Zhang, Xue Yang, Zheng Huang, Wei Sha, Effects of particle/matrix interface and strengthening mechanisms on the mechanical properties of metal matrix composites, Compos. Interfac. 21 (2014) 415–429, https://doi.org/10.1080/15685543.2014.872914.

[21] M. Boehm, P. Morin, T. Schmoelzer, D. Gentsch, R.A. Simon, A simple test method for the welding degradation of arcing contacts, in: ICEC 2014; the 27th International Conference on Electrical Contacts, Dresden, Germany, 2014, pp. 1–5.

[22] B. Miao, et al., The welding tendency of CuCr contact materials in vacuum, in: 24th ISDEIV 2010, 2010, pp. 265–268, https://doi.org/10.1109/DEIV.2010.5625754. Braunschweig, Germany.

[23] S. Xiu, R. Yang, J. Xue, J-x. Wang, J-y. Wang, Microstructure and properties of CuCr contact materials with different Cr content, Trans. Nonferrous Metals Soc. China 21 (2011) 389–393, https://doi.org/10.1016/S1003-6326(11)61612-9.

[24] R. Lin, L. Wang, W. Shi, J. Deng, S. Jia, Experimental investigation on triggered vacuum arc and erosion behavior under different contact materials, in: IEEE Transactions on Plasma Science, 2018, https://doi.org/10.1109/TPS.2018.2854715, 46.

[25] L. Yu, et al., Improvement of percussion welding characteristics of CuCr25 contact material by decreasing tensile strength, in: 2009 Proceedings of the 55th IEEE Holm Conference on Electrical Contacts, 2009, pp. 197–201, https://doi.org/10.1109/HOLM.2009.5284403. Vancouver, BC, Canada.

[26] C. Weichan, L. Shuhua, Z. Xiao, W. Xianhui, Y. Xiaohong, Effect of Fe on microstructures and vacuum arc characteristics of CuCr alloys, Int. J. Refract. Metals Hard Mater. 29 (2011) 237–243, https://doi.org/10.1016/j.ijrmhm.2010.10.012.

[27] J.B. Correia, H.A. Davies, C.M. Sellars, Strengthening in rapidly solidified age hardened Cu-Cr and Cu-Cr-Zr alloys, Acta Mater. 45 (1997) 177–190, https://doi.org/10.1016/S1359-6454(96)00142-5.

[28] P. Liu, B.X. Kang, X.G. Cao, et al., Strengthening mechanisms in a rapidly solidified and aged Cu-Cr alloy, J. Mater. Sci. 35 (2000), https://doi.org/10.1023/A:1004760014886.

[29] L. Varoto, J.-J. Blandin, P. Lhuissier, S. Roure, A. Papillon, M. Chosson, G. Martin, 3D microstructure characterization of Cu25Cr solid state sintered alloy using X-ray computed tomography and machine learning assisted segmentation, Mater. Char. 203 (2023), https://doi.org/10.1016/j.matchar.2023.113107.

[30] V. Boulos, L. Salvo, V. Fristot, P. Lhuissier, D. Houzet, Investigating performance variations of an optimized GPU-ported granulometry algorithm, in: 18th International European Conference on Parallel and Distributed Computing, Rhodes Island, Greece, 2012.

[31] E.F. Rauch, M. Véron, Automated crystal orientation and phase mapping in TEM, Mater. Char. 98 (2014), https://doi.org/10.1016/j.matchar.2014.08.010.

[32] A. Thomas, G. Fribourg, J.-J. Blandin, P. Lhuissier, R. Dendievel, G. Martin, Effect of the build orientation on mechanical and electrical properties of pure Cu fabricated by E-PBF, Addit. Manuf. 48 (2021), https://doi.org/10.1016/j.addma.2021.102393.

[33] W.C. Oliver, G.M. Pharr, An improved technique for determining hardness and elastic modulus using load and displacement sensing indentation experiments, J. Mater. Res. 7 (1992), https://doi.org/10.1557/JMR.1992.1564.

[34] D.J. Chakrabarti, D.E. Laughlin, The Cr-Cu (Chromium-Copper) system, Bulletin of Alloy Phase Diagrams 5 (1) (1984) 59–68.

[35] N. Chawla, Y.-L. Shen, Mechanical behavior of particle reinforced metal matrix composites, Adv. Eng. Mater. 3 (2001) 357–370, https://doi.org/10.1002/1527-2648(200106)3:6<357::AID-ADEM357>3.0.CO;2-I.

[36] Uwe Holzwarth, Hermann Stamm, Mechanical and thermomechanical properties of commercially pure chromium and chromium alloys, J. Nucl. Mater. 300 (2002) 161–177, https://doi.org/10.1016/S0022-3115(01)00745-0.

[37] T. Mochida, M. Taya, M. Obata, Effect of damaged particles on the stiffness of a particle/metal matrix composite, JSME international journal. Ser. 1, Solid mechanics, strength of materials 34 (1991) 187–193, https://doi.org/10.1299/jsmea1988.34.2_187.

[38] T. Mochizuki, T. Uesugi, Y. Takigawa, Prediction system for solid solubility limits of Ag-, Cu-, Al-, and Mg-based alloys using artificial neural networks and first-principles calculations, Mater. Trans. 61 (2020) 2083–2090, https://doi.org/10.2320/matertrans.MT-MBW2019010.

[39] T. Uesugi, K. Higashi, First-principles studies on lattice constants and local lattice distortions in solid solution aluminum alloys, Comput. Mater. Sci. 67 (2013) 1–10, https://doi.org/10.1016/j.commatsci.2012.08.037.

[40] R. Labusch, A statistical theory of solid solution hardening, Phys. Status Solidi 41 (1970) 659–669, https://doi.org/10.1002/pssb.19700410221.

[41] R.L. Fleischer, Substitutional solution hardening, Acta Metall. 11 (1963) 203–209, https://doi.org/10.1016/0001-6160(63)90213-X.

[42] J. Miettinen, V.-V. Visuri, T. Fabritius, Chromium-, copper-, molybdenum-, and nickel-containing thermodynamic descriptions of the Fe–Al– Cr–Cu–Mn–Mo–Ni–Si system for modeling the solidification of steels, Page 76, University of Oulu, Faculty of Technology, Process Metallurgy Research Unit Acta Univ. Oul. C 758 (2020). University of Oulu, P.O. Box 8000, FI-90014 University of Oulu, Finland.

[43] A. Chbihi, X. Sauvage, D. Blavette, Atomic scale investigation of Cr precipitation in copper, Acta Mater. 60 (2012) 4575–4585, https://doi.org/10.1016/j.actamat.2012.01.038.

[44] H. Sekine, R. Chent, A combined microstructure strengthening analysis of SiCp/Al metal matrix composites, Composites 26 (1995) 183–188, https://doi.org/10.1016/0010-4361(95)91381-E.

[45] N. Ramakrishnan, An analytical study on strengthening of particulate reinforced metal matrix composites, Acta Mater. 44 (1996) 69–77, https://doi.org/10.1016/1359-6454(95)00150-9.

[46] R.J. Arsenault, L. Wang, C.R. Feng, Strengthening of composites due to microstructural changes in the matrix, Acta Metall. Mater. 39 (1991) 47–57, https://doi.org/10.1016/0956-7151(91)90327-W.

[47] H.L. Cox, The elasticity and strength of paper and other fibrous materials, Br. J. Appl. Phys. 3 (1952), https://doi.org/10.1088/0508-3443/3/3/302.

[48] N.A. Dubrovinskaia, L.S. Dubrovinsky, S.K. Saxena, Thermal expansion of Chromium (Cr) to melting temperature, Calphad 21 (1997) 497–508, https://doi.org/10.1016/S0364-5916(98)00007-8.

[49] K. Wang, R.R. Reeber, Thermal expansion of copper, High Temp. Mater. Sci. 35 (1996).

[50] A.J. Ardell, Precipitation hardening, Metall. Trans. A 16 (1985) 2131–2165, https://doi.org/10.1007/BF02670416.

[51] Y. Jin, K. Adachi, K. Takeuchi, et al., Ageing characteristics of Cu–Cr in-situ composite, J. Mater. Sci. 33 (1998) 1333–1341, https://doi.org/10.1023/A:1004310700846.

[52] S.D. Brown, R.B. Biddulph, P.D. Wilcox, A strength–porosity relation involving different pore geometry and orientation, J. Am. Ceram. Soc. 47 (1964) 320–322, https://doi.org/10.1111/j.1151-2916.1964.tb12993.x.

[53] F. Mirza, D. Chen, A unified model for the prediction of yield strength in particulate-reinforced metal matrix nanocomposites, Materials 8 (2015) 5138–5153, https://doi.org/10.3390/ma8085138.

[54] J. Le, Y. Han, M. Fang, S. Li, G. Huang, J. Mao, C.J. Boehlert, W. Lu, A universal shear-lag model for accurate assessment of whisker load-transfer strengthening in metal matrix composites, Compos. B Eng. (2022) 247, https://doi.org/10.1016/j.compositesb.2022.110317.

[55] Y. Jin, K. Adachi, T. Takeuchi, H.G. Suzuki, Cu precipitation in Cr ribbon of Cu-15 wt % Cr in situ composite, Appl. Phys. Lett. 2 (September 69) (1996) 1391–1392, https://doi.org/10.1063/1.117591.